

A Power-Loss-Dependent Inductance Model for Ferrite-Core Power Inductors in Switch-Mode Power Supplies

Alberto Oliveri, *Member, IEEE*, Giulia Di Capua, *Member, IEEE*, Kateryna Stoyka, Matteo Lodi, *Student Member, IEEE*, Marco Storace, *Senior Member, IEEE*, and Nicola Femia, *Senior Member, IEEE*

Abstract—This paper proposes a new modeling approach for ferrite-core (FC) power inductors used in switch-mode power supplies (SMPSs). In particular, a novel power-loss-dependent inductance behavioral model is proposed, whose parameters can be identified through a limited set of proper experimental measurements of inductor current and voltage. Unlike conventional thermal modeling approaches, which require information on core temperature, the proposed behavioral model relies only on easily measurable quantities. The model is also suitable for being implemented in circuit simulators. By comparing PSIM simulations and experimental measurements on a buck converter for commercial FC inductors, we show that the model allows a reliable prediction of the steady-state inductor current, under different SMPS working conditions.

Index Terms—Behavioral nonlinear model, high power density, magnetic saturation, power loss.

I. INTRODUCTION

THE achievement of higher and higher power density levels is a main concern in Switch-Mode Power Supply (SMPS) design [1], especially in the aerospace and automotive domains, where weight and size are major constraints due to the current trend towards more electric vehicles, which require more power electronics on-board. Although integrated hardware solutions, such as power modules, systems-in-package and systems-on-chip [2], allow to reduce the impact of power devices on SMPSs weight and size, power magnetic components often remain the largest devices in high-frequency discrete power supplies, and their minimization is mandatory to step-up the power density of SMPSs [3].

Ferrite-Core (FC) inductors are extensively employed in SMPSs, owing to their low cost and low power loss. Their inductance drops quite sharply as the current increases,

because of magnetic core saturation. For this reason, in SMPS design FC inductors are generally selected to ensure that in the worst-case condition the peak current determines an inductance drop limited within about 20% of its nominal value. As a consequence, FC inductors are often oversized [4].

Recent studies [4]–[7] show that it is possible to use smaller FC inductors working with worst-case peak current falling in the region beyond 20% of inductance drop, by ensuring that they satisfy the overall design specifications. In this case, we say that the inductors work in *Sustainable Saturation Operation* (SSO), which enables the achievement of more compact SMPSs [4]. A reliable SSO-based design requires the development of novel inductor models, which is the main motivation of this paper. When dealing with FC inductors, it is important to consider that the region wherein the devices sharply saturate drifts towards lower current values when the core temperature increases [8]. This thermal drift could be modeled starting from the physical and geometrical characteristics of the inductor, if known. Unfortunately, this information is not disclosed for commercial FC inductors used in the majority of SMPSs. Therefore, new behavioral models of FC inductors are needed to reliably estimate power loss and inductance in high-power-density SMPSs exploiting SSO, including the thermal drift of the saturation region.

In this framework, new methods for the identification of inductor saturation curves [9], [10] and new models to properly handle the nonlinear behavior of FC inductors in SSO [11] (including inductor hysteresis [12] and temperature [13]) have been proposed in the last years. The main limits of these models are that they either depend on the inductor core temperature [12], [13], which is difficult to measure, or do not take into account all the SMPS working conditions [10].

The novel FC inductors modeling approach presented in this paper is based on the assumption that the *core temperature* is not an *input* variable in the inductor model, but rather an *output*. Usually, manufacturers only provide thermal models regarding the impact of the *ambient temperature* on the inductance [14]. Actually, the *core temperature* depends on the heat transfer characteristics and impedance of the component, on the current through it, and on several environmental elements, including the circuit board, the soldering connection and the surrounding power components. In particular,

This work was supported in part by the University of Salerno (grant 300638FFABR18DICAPUA) and in part by the University of Genoa. A. Oliveri, M. Lodi, and M. Storace are with the Department of Electrical, Electronics and Telecommunication Engineering and Naval Architecture, University of Genoa, 16145 Genoa, Italy (e-mail: marco.storace@unige.it).

G. Di Capua, K. Stoyka, and N. Femia are with the Department of Information and Electrical Engineering and Applied Mathematics, University of Salerno, 84084 Fisciano, Italy.

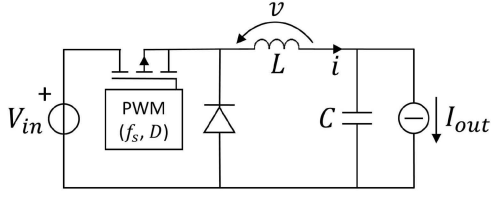


Fig. 1. Schematic of a buck converter.

for a given setup and ambient temperature, different SMPS operating conditions generating the same power loss lead to the same core temperature. Based on this premise, this paper introduces a new parametric inductance model valid at electrical and thermal steady state. Following the fundamentals of circuit theory approach [15], the proposed behavioral nonlinear inductance model depends on easily measurable variables and parameters, *i.e.*, the inductor current and its total power loss. The new model is suitable for predicting the inductance under any SMPS working condition, thus generalizing previous models proposed in [10] and [16]. Moreover, for a specific FC inductor, the model parameters can be identified based on a limited set of experimental measurements of voltage and current. Validation on a large set of measurements allows us to assess model accuracy and generalization capability. PSIM simulations of an SMPS based on two identified commercial FC inductors' models show that the predicted current waveforms are in good agreement with the experimental measurements. The model accuracy is assessed by using multiple samples of the same inductor and inductors with the same magnetic core but different inductance.

The paper is organized as follows. In Section II, the proposed inductance model is presented. Section III describes how the experimental datasets for model identification are obtained. Simulation results and comparisons with measurements are shown in Section IV, before discussing results and drawing some conclusions in Section V.

II. PROPOSED INDUCTANCE MODEL

In this paper, the buck converter shown in Fig. 1 is adopted as a reference case study, but the findings relative to FC inductors modeling have general conceptual validity, and can be applied to whatever converter topology. Let $w = [V_{in}, I_{out}, f_s, D]$ be the vector of parameters determining the SMPS operating condition, where V_{in} is the input voltage, I_{out} is the output current, f_s is the switching frequency and D is the duty cycle of the pulse-width modulation driving signal. Given the operating condition w , the steady-state inductor current $i(t)$ and voltage $v(t)$ are periodic waveforms of period $T_s = \frac{1}{f_s}$.

At steady state, the magnetic flux Φ depends on inductor current i and core temperature T , as shown in Fig. 2, where the Φ versus i curves at steady state correspond to different core temperatures $T_2 > T_1$. This figure evidences the presence of marginal hysteresis in the $\Phi(i)$ characteristics. As a matter of fact, in commercial FC inductors, gapped cores determine a flattening of hysteresis loops. For this reason, the hysteresis is not taken into account in the proposed inductance model.

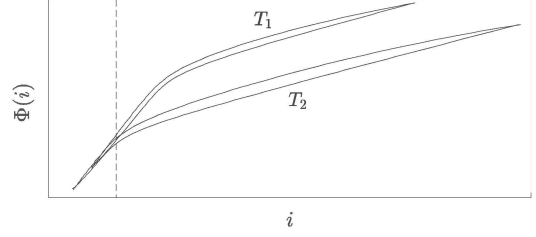


Fig. 2. Φ versus i hysteretic curves. The magnetic flux is obtained by integrating with respect to time the experimental waveforms of inductor voltage, measured over the switching period at steady state for the same inductor, at two different core temperatures $T_2 > T_1$.

Unfortunately, the core temperature T is not easy to measure. Given the ambient temperature T_a , different SMPS operating conditions generating the same average power loss p lead to the same core temperature. The power loss is easier to measure and a behavioral model has been recently proposed [16], which relates p to the SMPS working condition w . Therefore, p is considered as input of the model herein proposed, instead of core temperature T . Accordingly, the inductor voltage v is related to the flux Φ by the following relationship:

$$v(t) = \frac{\partial}{\partial t} \Phi(i; p) \quad (1)$$

At steady state, p is constant and Eq. (1) can be recast as

$$v(t) = \frac{\partial}{\partial i} \Phi(i; p) \frac{d}{dt} i(t) = L(i; p) \frac{d}{dt} i(t) \quad (2)$$

where $L(i; p) = \frac{\partial}{\partial i} \Phi(i; p)$ is the *incremental inductance* [15] (in the following, simply referred to as inductance) for the steady-state solution related to w . The plots in Fig. 2 show that the slope of $\Phi(i)$ is approximately constant for low current values (on the left of the dashed line). As i increases, the curves exhibit a knee and become again approximately linear, with a lower slope. This behavior is due to magnetic saturation, which is taken into account in the proposed inductance model.

A. Power-Loss-Dependent Inductance Model

Fig. 3 shows an example of FC inductor saturation curves provided by manufacturers at different ambient temperatures. These experimental curves show that FC inductors saturate at lower currents as the ambient temperature increases. This kind of L vs I characterization is normally obtained by sweeping the DC component of a small-amplitude sinusoidal input [17]. Therefore, given an ambient temperature, each point along the related inductance curve corresponds to a different core temperature, as the power loss depends mainly on the DC component of the current. To overcome this limitation, in this paper we propose a novel modeling approach.

For a given ambient temperature, the inductance of FC inductors can be expressed as a function of both the current i and the average power loss p :

$$L(i; p) = L^{low}(p) + \frac{L^{high}(p) - L^{low}(p)}{2} \times \left\{ 1 - \frac{2}{\pi} \text{atan} \left\{ \sigma(p) [i - I^*(p)] \right\} \right\} \quad (3)$$

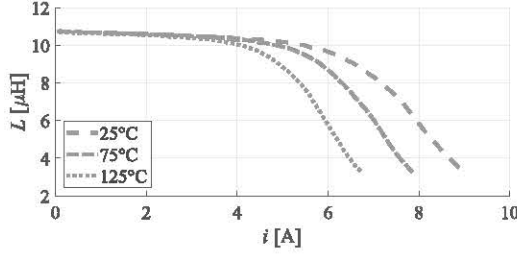


Fig. 3. L vs i experimental curves of Coilcraft MSS1260-103 inductor at three different ambient temperatures [18].

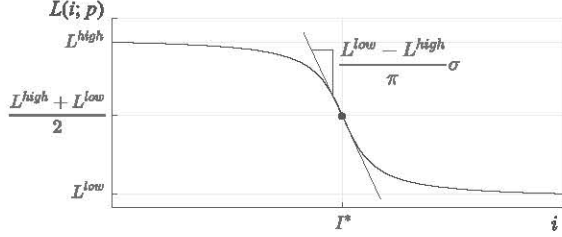


Fig. 4. L vs i curve at given power loss and ambient temperature.

which generalizes the model discussed in [11]. Fig. 4 shows a plot of the function $L(i; p)$. The parameters L^{high} and L^{low} are the horizontal asymptotes of the curve, I^* is the abscissa of its inflection point, and σ (> 0) is proportional to the slope of the curve in I^* . The curves of Fig. 3 highlight that the ambient temperature mainly influences their horizontal position, which is associated to the abscissa I^* of the inflection point of the curve shown in Fig. 4. The core temperature increases if we increase the ambient temperature (for a fixed power loss) or we increase the power loss (for a fixed ambient temperature). Therefore, we assume that L^{high} , L^{low} and σ are fixed, whereas I^* is dependent on the power loss p :

$$L^{high} = x_1; L^{low} = x_2; \sigma = x_3; I^* = x_4 p + x_5 \quad (4)$$

where $\mathbf{x} = [x_1 \ x_2 \ x_3 \ x_4 \ x_5]^T$ is a vector of fitting coefficients. The average power loss p can be either measured or estimated through any reliable power loss model.

We remark that model (3) is applied in this paper to soft-ferrite inductors with gapped magnetic core. The air gap has mainly the effect of reducing L^{high} and increasing I^* [19].

B. Model Fitting

Given a working condition w and a time interval $[t_0, t]$, from Eq. (2) it follows:

$$\underbrace{\int_{t_0}^t v(\tau) d\tau}_{\Phi(t)} = \underbrace{\int_{i(t_0)}^{i(t)} L(i'; p) di'}_{\hat{\Phi}(i(t); p)} \quad (5)$$

The experimental magnetic flux $\Phi(t)$ in Eq. (5) can be computed using the measurements of the inductor voltage, whereas the analytical magnetic flux $\hat{\Phi}(i(t); p)$ can be computed by

integrating Eq. (3), thus obtaining:

$$\begin{aligned} \hat{\Phi}(i(t); p) &= \int_{i(t_0)}^{i(t)} L(i'; p) di' \\ &= \left\{ \frac{L^{high} + L^{low}}{2} i + \frac{L^{high} - L^{low}}{2\pi\sigma} \log 1 + \sigma^2 (i - I^*)^2 \right. \\ &\quad \left. + \frac{L^{low} - L^{high}}{\pi} (i - I^*) \operatorname{atan} [\sigma (i - I^*)] \right\} \Big|_{i=i(t_0)}^{i=i(t)} \end{aligned} \quad (6)$$

Given K different working conditions w_k ($k = 1, \dots, K$), let $v_k(t)$, $i_k(t)$, $\Phi_k(t)$ and p_k be the steady-state inductor voltage, current, magnetic flux and average power loss related to the k -th working condition, respectively. If v_k and i_k are measured in N time instants t_n ($n = 1, \dots, N$), the optimal coefficient vector \mathbf{x}^* can be obtained by solving the following nonlinear optimization problem:

$$\mathbf{x}^* = \arg \min_{\mathbf{x}} \sum_{k=1}^K \sum_{n=1}^N [\Phi_k(t_n) - \hat{\Phi}(i_k(t_n); p_k)]^2 \quad (7)$$

where $\Phi_k(t_n) = \int_{t_0}^{t_n} v_k(\tau) d\tau$, $\hat{\Phi}(i_k(t_n); p_k)$ is computed through Eq. (6), and the inductance parameters L^{high} , L^{low} , σ and I^* are given by Eq. (4). The power loss p_k can be either measured or estimated through a model expressing the steady-state average power loss p for FC inductors as a function of the operating condition w . Here, we use the model summarized hereinafter and discussed in [16]. Solving the optimization problem (7) yields the vector of fitting coefficients \mathbf{x}^* characterizing the inductor model for different operating conditions.

C. Model Accuracy Evaluation

Given a set of experimental measurements (the procedure to obtain these data is described in Section III), the optimization problem (7) can be solved, and the resulting optimal vector \mathbf{x}^* can be used to compute the arctangent parameters (4). Then, the inductance $L(i; p)$ can be evaluated for any value of i and p , through Eq. (3). According to Eq. (2), integrating numerically the ratio $\hat{v}_k(t)/L(\hat{i}_k(t); p_k)$ over the time interval $[t_0, t_n]$ provides the inductor current value $\hat{i}_k(t_n)$ at time t_n , under the k -th operating condition:

$$\hat{i}_k(t_n) = \hat{i}_k(t_0) + \int_{t_0}^{t_n} \frac{\hat{v}_k(t)}{L(\hat{i}_k(t); p_k)} dt \quad (8)$$

The estimated initial inductor current $\hat{i}_k(t_0)$ is assumed to be equal to the corresponding experimental initial inductor current $i_k(t_0)$. The function $\hat{v}_k(t)$ can be obtained through an interpolation of samples $v_k(t_n)$. The results of Section IV have been obtained by using a simple piecewise-affine interpolation. For the k -th operating condition, the estimated current ripple can be obtained as $\hat{\Delta}_k = \max_j \hat{i}_k(t_j) - \min_j \hat{i}_k(t_j)$ (for $k = 1, \dots, K$). The fitting accuracy can be evaluated by means

of three percent errors E_k^Φ , E_k^I and E_k^Δ , defined as follows:

$$E_k^\Phi = 100 \sqrt{\frac{1}{N} \frac{\sum_{n=1}^N [\Phi_k(t_n) - \hat{\Phi}(i_k(t_n); p_k)]^2}{[\max_n \Phi_k(t_n) - \min_n \Phi_k(t_n)]^2}} \quad (9)$$

$$E_k^I = 100 \sqrt{\frac{1}{N} \frac{\sum_{n=1}^N [i_k(t_n) - \hat{i}_k(t_n)]^2}{[\max_n i_k(t_n) - \min_n i_k(t_n)]^2}} \quad (10)$$

$$E_k^\Delta = 100 \frac{|\Delta_k - \hat{\Delta}_k|}{\Delta_k} \quad (11)$$

For each dataset, the errors (9)-(11) and the corresponding mean value $\bar{E}^{(\Phi, I, \Delta)}$, standard deviation $\sigma^{(\Phi, I, \Delta)}$ and maximum value $E_M^{(\Phi, I, \Delta)}$ can be calculated over the K operating conditions.

D. Inductor Power Loss Model

The FC inductors power loss p is determined by magnetic core loss and winding loss. The magnetic core loss, in turn, includes hysteresis loss, eddy current loss and residual loss [20]. For commercial pre-assembled power inductors working in real SMPSs, it is not possible to measure or separate core (AC contribution only) and winding (DC+AC contributions) losses, especially if windings arrangement or magnetic material are not disclosed by the manufacturer, as it usually happens. Alternatively, the FC inductor power loss p can be evaluated as the sum of a DC term and an AC term, both depending on the SMPS working conditions:

$$p(w) = P_{dc}(w) + P_{ac}(w) \quad (12)$$

The DC loss P_{dc} is due to the average inductor current I_{dc} :

$$P_{dc}(w) = R_{dc} I_{dc}^2 \quad (13)$$

where R_{dc} is the DC winding resistance, measurable starting from the DC inductor current and voltage, and I_{dc} coincides with I_{out} in the considered buck converter.

The AC loss P_{ac} , including the contributions of winding and magnetic core (hysteresis, eddy currents, residual), is evaluated by means of a behavioral model for FC power inductors operating in SMPS applications [16], identified by means of an evolutionary algorithm applied to a large experimental dataset. The resulting AC loss formula P_{ac} is:

$$P_{ac}(w) = c_0 e^{-c_1 f_s} (V_{on} D)^{c_2} + c_3 (V_{on} D)^2 \quad (14)$$

where $V_{on} = V_{in}(1 - D)$ is the inductor voltage during the on-time interval DT_s for the considered buck converter, and terms c_j ($j = 0, \dots, 3$) are functions of I_{dc} , dependent on coefficients C_{jk} ($k = 0, \dots, 3$):

$$c_j(I_{dc}) = C_{j0} e^{C_{j1} I_{dc}} + C_{j2} I_{dc} + C_{j3} \quad (15)$$

III. CASE STUDIES

The case studies discussed in this paper are referred to commercial power inductors with different ferrite materials and core types. In particular, two Coilcraft FC inductors are considered: a 10 μ H shielded MSS1260-103 (inductor #1) and

TABLE I
INDUCTORS PARAMETERS

#	Part Number	Size [mm ³]	L_{nom} [μ H]	R_{dc} [m Ω]	I_{sat} [A] 30% drop
1	MSS1260-103	12.0x12.0x6.0	10	24	7.40
2	DO3316T-103	13.2x9.9x6.4	10	34	3.80

TABLE II
COEFFICIENTS OF THE AC POWER LOSS BEHAVIORAL MODEL

Inductor #1 (MSS1260-103)				
C_{jk}	$k = 0$	$k = 1$	$k = 2$	$k = 3$
$j = 0$	5.76E-04	1.70E+00	-2.71E+00	3.86E+01
$j = 1$	2.20E-06	1.23E+00	-4.16E-04	6.78E-03
$j = 2$	9.65E-14	4.12E+00	-5.39E-03	2.05E+00
$j = 3$	2.36E+01	1.36E-01	-5.23E+00	-1.78E+01
Inductor #2 (DO3316T-103)				
C_{jk}	$k = 0$	$k = 1$	$k = 2$	$k = 3$
$j = 0$	2.00E-08	5.59E+00	-6.21E+00	8.28E+01
$j = 1$	1.61E-09	3.75E+00	-4.39E-04	6.32E-03
$j = 2$	4.09E-11	5.94E+00	-1.04E-02	1.88E+00
$j = 3$	4.33E-07	4.02E+00	-2.63E-01	4.72E+00

a 10 μ H unshielded DO3316T-103 (inductor #2). The main characteristics of these inductors are listed in Table I, where I_{sat} represents the DC current causing the 30% inductance drop with respect to the nominal inductance of the device at 25°C. The AC power loss model coefficients C_{jk} ($j = 0, \dots, 3$, $k = 0, \dots, 3$) for inductors #1 and #2 are listed in Table II.

For each inductor, the experimental dataset including inductor current $i_k(t)$, voltage $v_k(t)$ and power loss p_k ($k = 1, \dots, K$) has been collected by means of the MADMIX system [21]. This automated measurement set-up allows to perform high-speed sampling of the inductor voltage and current under typical hard-switched conditions characterizing SMPSs.

Two datasets have been constructed for inductor #1 and #2, labeled as \mathcal{S}_{11} and \mathcal{S}_{12} , respectively, consisting of $K = 880$ different operating conditions, corresponding to all the combinations of parameters V_{in} , I_{out} , f_s and D listed in the upper part of Table III. The maximum sampling frequency of MADMIX is 1GHz, which allows to obtain up to 2000 voltage and current samples per period, with a switching frequency $f_s = 500$ kHz (worst case). However, a so high resolution is not necessary to identify the proposed inductance model. In this paper, for each operating condition, $N = 200$ samples of voltage and current waveforms have been acquired per period, thus obtaining values $v_k(t_n)$ and $i_k(t_n)$, with $n = 1, \dots, N$ and $k = 1, \dots, K$. Also the average power loss p_k has been experimentally measured by the MADMIX system.

The experimental datasets cover the following ranges of average power p_k and current ripple Δ_k :

- inductor #1: $p_k \in [0.18, 1.89]$ W, $\Delta_k \in [0.20, 6.61]$ A;
- inductor #2: $p_k \in [0.12, 1.52]$ W, $\Delta_k \in [0.23, 6.13]$ A.

Two subsets, labeled as \mathcal{S}_{21} and \mathcal{S}_{22} , have been extracted from the original datasets \mathcal{S}_{11} and \mathcal{S}_{12} , with the operating conditions given by the $K = 24$ combinations of parameters V_{in} , I_{out} , f_s and D provided in the lower part of Table III. These combinations involve the operating conditions with large average currents and current ripples.

TABLE III

OPERATING CONDITIONS USED IN DATASETS \mathcal{S}_{11} , \mathcal{S}_{12} , \mathcal{S}_{21} , AND \mathcal{S}_{22}

Dataset	\mathcal{S}_{11} (inductor #1)	\mathcal{S}_{12} (inductor #2)
$V_{in}[V]$	{6, 8, 10, 12}	{6, 8, 10, 12}
$I_{out}[A]$	{3, 3.5, 4, 4.5, 5, 5.5, 6, 6.5, 7, 7.5, 8}	{2, 2.25, 2.5, 2.75, 3, 3.25, 3.5, 3.75, 4, 4.25, 4.5}
$f_s[kHz]$	{200, 300, 400, 500}	{200, 300, 400, 500}
D	{0.2, 0.35, 0.5, 0.68, 0.8}	{0.2, 0.35, 0.5, 0.68, 0.8}
Subset	\mathcal{S}_{21} (inductor #1)	\mathcal{S}_{22} (inductor #2)
$V_{in}[V]$	{6, 12}	{6, 12}
$I_{out}[A]$	{5.5, 6, 6.5, 7, 7.5, 8}	{3.25, 3.5, 3.75, 4, 4.25, 4.5}
$f_s[kHz]$	{200, 300}	{200, 300}
D	0.5	0.5

TABLE IV

STATISTICS OF THE ERRORS FOR ALL PERFORMED TESTS

Inductor #1 (MSS1260-103)			
Dataset	\bar{E}^Φ [%]	σ^Φ [%]	E_M^Φ [%]
\mathcal{S}_{11} (case a)	1.41	0.29	2.62
\mathcal{S}_{21} (case b)	1.42	0.29	2.53
Dataset	\bar{E}^I [%]	σ^I [%]	E_M^I [%]
\mathcal{S}_{11} (case a)	2.07	0.91	7.65
\mathcal{S}_{21} (case b)	2.15	0.92	6.80
Dataset	\bar{E}^Δ [%]	σ^Δ [%]	E_M^Δ [%]
\mathcal{S}_{11} (case a)	2.60	2.36	17.04
\mathcal{S}_{21} (case b)	2.56	2.17	13.36
Inductor #2 (DO3316T-103)			
Dataset	\bar{E}^Φ [%]	σ^Φ [%]	E_M^Φ [%]
\mathcal{S}_{12} (case a)	2.24	0.30	4.20
\mathcal{S}_{22} (case b)	2.50	0.51	3.70
Dataset	\bar{E}^I [%]	σ^I [%]	E_M^I [%]
\mathcal{S}_{12} (case a)	3.44	1.41	11.36
\mathcal{S}_{22} (case b)	3.92	1.61	10.47
Dataset	\bar{E}^Δ [%]	σ^Δ [%]	E_M^Δ [%]
\mathcal{S}_{12} (case a)	3.54	3.49	21.73
\mathcal{S}_{22} (case b)	5.26	3.18	18.46

IV. MODELING RESULTS

In this section, the FC inductors models obtained with the proposed approach are presented and discussed.

A. Inductor Simulation

The problem (7) has been solved on datasets \mathcal{S}_{11} and \mathcal{S}_{12} (case a) first, and then on subsets \mathcal{S}_{21} and \mathcal{S}_{22} (case b). In both cases, the error statistics are computed on datasets \mathcal{S}_{11} , \mathcal{S}_{12} . The results are shown in Table IV. It can be noticed that the error variation for case b is negligible, even if only $K = 24$ operating conditions are used to train the model. This is due to the fact that datasets \mathcal{S}_{21} and \mathcal{S}_{22} contain the operating conditions with the largest average currents and current ripples, i.e., the conditions wherein the inductor current spans a wider portion of the L vs i curve (see Eq. (3) and Fig. 4). This suggests that it is not necessary to employ operating conditions with low current values to achieve a good model fitting. From a practical viewpoint, this means that only a *limited set* of proper measurements are enough to obtain an accurate model. The resulting coefficient vectors \mathbf{x}^* for inductors #1 and #2 are shown in Table V. The arctangent parameters L^{high} , L^{low} , σ and I^* can be obtained by substituting \mathbf{x}^* and the measured power loss p_k (corresponding to w_k) in Eq. (4). The resulting arctangent functions for the two inductors are shown in Fig. 5, for all the 880 operating conditions.

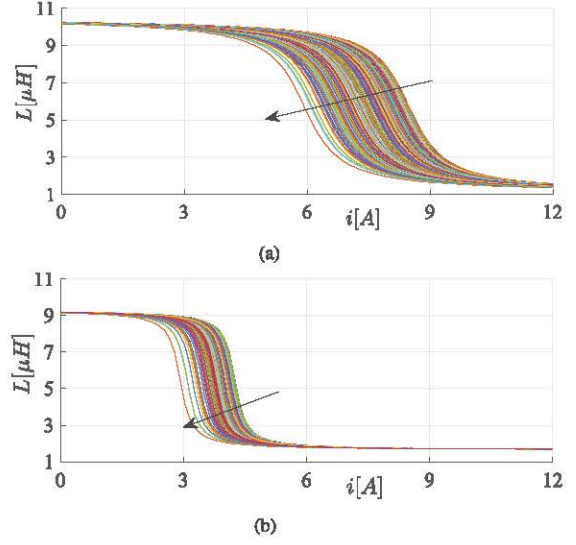


Fig. 5. Families of $L(i)$ characteristics for inductors #1 (a) and #2 (b). The arrows indicate the increasing direction of p .

TABLE V

COEFFICIENT VECTORS \mathbf{x}^* FOR INDUCTORS #1 AND #2

Inductor	\mathbf{x}^*
#1	[10.48 μ H, 1.02 μ H, 1.54A $^{-1}$, -1.52AW $^{-1}$, 8.78A]
#2	[9.30 μ H, 1.63 μ H, 5.25A $^{-1}$, -0.95AW $^{-1}$, 4.37A]

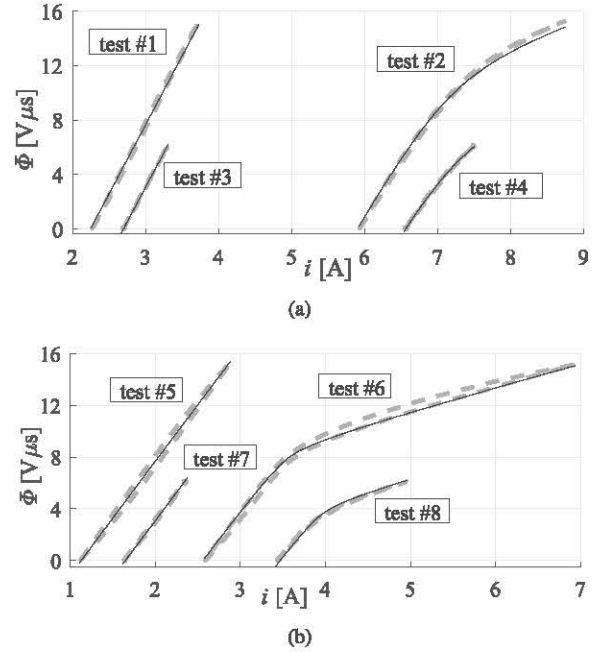


Fig. 6. Experimental magnetic flux Φ vs i (gray dashed lines) and analytical magnetic flux $\hat{\Phi}$ vs i (black lines) for inductor #1 (a) and inductor #2 (b).

The shapes of the inductance curves of the two inductors are quite different because of the different core. For inductor #1 (shielded core) the inductance drop is smoother and occurs at a higher current with respect to inductor #2 (unshielded core), for which the modeling error is slightly higher (see Table IV). Similar considerations hold also for other

TABLE VI
TEST CONDITIONS: $V_{in} = 12\text{ V}$, $D = 0.5$

Inductor #1 (MSS1260-103)			Inductor #2 (DO3316T-103)		
Test #	f_s [kHz]	I_{out} [A]	Test #	f_s [kHz]	I_{out} [A]
1	200	3	5	200	2
2	200	7	6	200	4
3	500	3	7	500	2
4	500	7	8	500	4

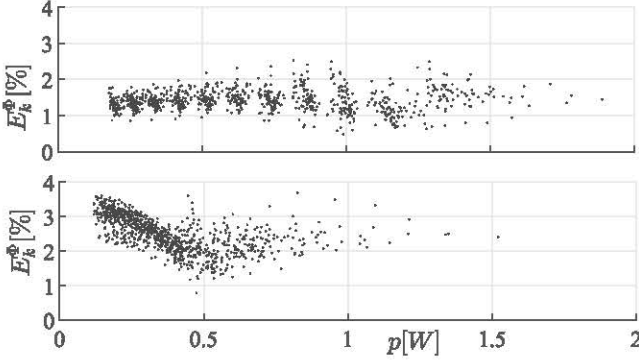


Fig. 7. Error E_k^Φ vs power loss p obtained with the proposed model for inductor #1 (top panel) and inductor #2 (bottom panel).

inductors with the same core but different nominal inductance, as shown in Appendix ???. It is worth remarking that the L_{nom} value declared in the devices datasheet is subjected to about 10%-20% uncertainty. For instance, Fig. 5(b) and Table V point out that the real inductance of inductor #2 for low currents is about $9\mu\text{H}$, whereas the nominal inductance is $10\mu\text{H}$.

Fig. 6 shows the experimental magnetic flux Φ versus the current i (gray dashed lines), obtained in the test conditions summarized in Table VI for the two investigated FC inductors. These tests include low and high switching frequency values, as well as low and high output current values. The plots also show the analytical magnetic flux $\hat{\Phi}$ versus the current i (black lines), obtained by using Eq. (6) and the coefficient vector \mathbf{x}^* given in Table V. The analytical magnetic flux $\hat{\Phi}$ fits very well the experimental one for all the analyzed tests.

The errors E_k^Φ versus power loss p are shown in Fig. 7, for the two analyzed inductors. The results highlight that the proposed model provides a good fitting accuracy over a wide range of operating conditions, even by determining the model parameters (4) over a limited set of conditions with large average currents and current ripples.

B. Multiple Sample Testing

To enhance the generality of the proposed inductance modeling approach and check the results deviation, two further samples have been tested for the MSS1260-103 and DO3316T-103 inductors, by performing measurements under the operating conditions given by all the combinations of parameters V_{in} , I_{out} , f_s and D used to obtain subsets S_{21} and S_{22} (see bottom part of Table III). In a first test, the coefficient vectors shown in Table V (trained on sample 1) have been used also to model samples 2 and 3 and to compute errors E_k^Φ

TABLE VII
STATISTICS OF THE ERRORS FOR THREE SAMPLES
WITH MODEL TRAINED ON SAMPLE 1

Inductor #1 (MSS1260-103)			
Sample	\bar{E}^Φ [%]	σ^Φ [%]	E_M^Φ [%]
1	1.42	0.27	1.89
2	3.65	2.06	7.19
3	1.74	0.50	3.25

Inductor #2 (DO3316T-103)			
Sample	\bar{E}^Φ [%]	σ^Φ [%]	E_M^Φ [%]
1	2.28	0.29	2.92
2	2.59	0.80	4.62
3	2.63	0.83	4.72

TABLE VIII
COEFFICIENT VECTORS \mathbf{x}^* FOR INDUCTOR #1 AND #2
WITH MODEL TRAINED ON ALL SAMPLES

Inductor	\mathbf{x}^*
#1	[10.81 μH , 0.84 μH , 1.33A $^{-1}$, -1.50AW $^{-1}$, 8.59A]
#2	[9.62 μH , 1.60 μH , 4.88A $^{-1}$, -0.93AW $^{-1}$, 4.28A]

TABLE IX
STATISTICS OF THE ERRORS FOR THREE SAMPLES
WITH MODEL TRAINED ON ALL SAMPLES

Inductor #1 (MSS1260-103)			
Sample	\bar{E}^Φ [%]	σ^Φ [%]	E_M^Φ [%]
1	2.08	0.70	3.64
2	2.32	1.16	4.51
3	1.65	0.49	3.12

Inductor #2 (DO3316T-103)			
Sample	\bar{E}^Φ [%]	σ^Φ [%]	E_M^Φ [%]
1	2.71	0.32	3.31
2	2.22	0.36	3.19
3	2.24	0.42	3.24

for the $K = 24$ considered operating conditions. The corresponding statistics are shown in Table VII. We notice that for inductor #1 the modeling error for sample 2 is significantly higher than for the other two samples, which confirms that there may be a significant variability between different samples of the same component. In a second test, the inductance model coefficients for each inductor have been identified by exploiting the measurements on all samples. The corresponding optimal coefficient vectors are shown in Table VIII. The error statistics are listed in Table IX and point out a higher homogeneity in the modeling errors across the samples. These tests confirm that the proposed model is quite general and provides limited fitting errors, also for multiple inductor samples subjected to manufacturing tolerances.

C. SMPS Circuit Simulations

The results of SMPS circuit simulations obtained by using the proposed model have been compared with experimental measurements, in order to validate the accuracy of the inductance modeling approach. The open-loop buck topology shown in Fig. 1 has been implemented in the power electronics simulator PSIM. At a fixed working condition w_k , the zero-order-hold discretization of Eq. (8) yields

$$\hat{i}_k(t_{n+1}) = \hat{i}_k(t_n) + \frac{(t_{n+1} - t_n)\hat{v}_k(t_n)}{L(\hat{i}_k(t_n); p_k)} \quad (16)$$

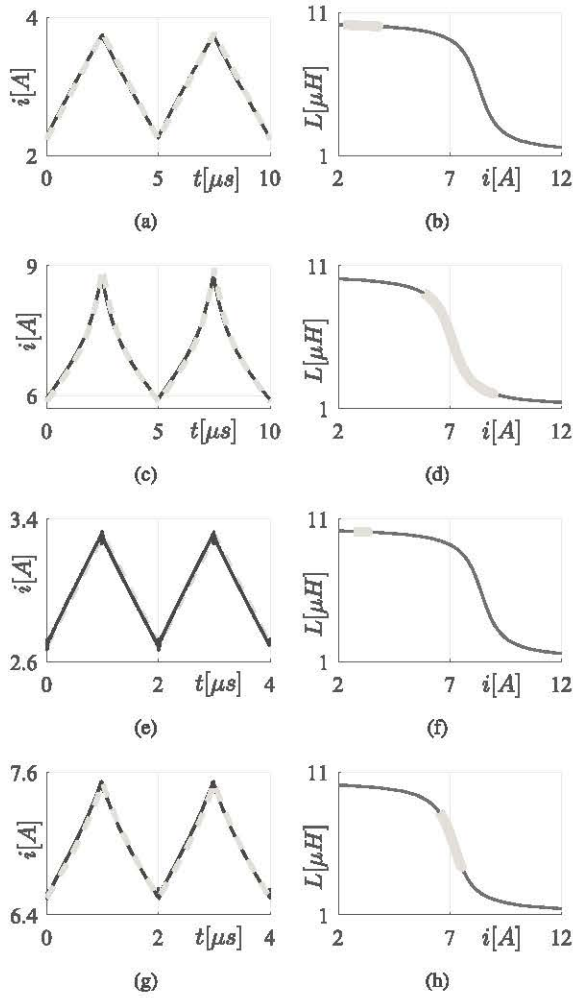


Fig. 8. MSS1260-103 inductor. Left: experimental inductor current waveforms (black solid lines) vs PSIM simulations (gray dashed lines). Right: simulated inductance vs current profiles (black) and relevant current ripple (gray). (a) current vs time, test #1. (b) inductance vs current, test #1. (c) current vs time, test #2. (d) inductance vs current, test #2. (e) current vs time, test #3. (f) inductance vs current, test #3. (g) current vs time, test #4. (h) inductance vs current, test #4.

In particular, the inductor has been implemented in PSIM as a *current-controlled current source*, whose driving signal is the result of the right-hand-side of Eq. (16), run-time computed by means of a C-block. The inputs to the C-block are:

- the SMPS operating condition $w_k = [V_{in}, I_{out}, f_s, D]$;
- the optimal coefficient vector \mathbf{x}^* (see Table V);
- the coefficients R_{dc} and C_{jk} (see Tables I and II);
- the samples of the simulated inductor voltage $\hat{v}_k(t_n)$ and current $i_k(t_n)$.

For each k and n , the C-block computes:

- the inductor average power loss \hat{p}_k (Eq. (12));
- the parameter I^* (Eq. (4));
- the inductance $L(i_k(t_n); \hat{p}_k)$ (Eq. (3));
- the next current sample $i_k(t_{n+1})$ (Eq. (16)).

The tests conditions summarized in Table VI have been adopted in PSIM. The SMPS simulations have been performed with a constant sampling time of 10 ns for both inductors #1 and #2, and validated by comparison with

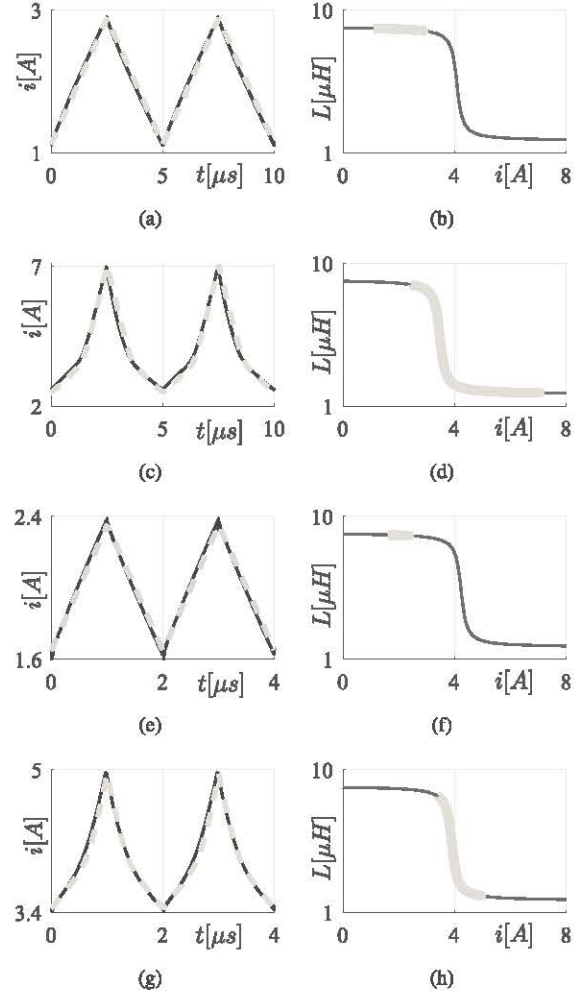


Fig. 9. DO3316T-103 inductor. Left: experimental inductor current waveforms (black solid lines) vs PSIM simulations (gray dashed lines). Right: simulated inductance vs current profiles (black) and relevant current ripple (gray). (a) current vs time, test #5. (b) inductance vs current, test #5. (c) current vs time, test #6. (d) inductance vs current, test #6. (e) current vs time, test #7. (f) inductance vs current, test #7. (g) current vs time, test #8. (h) inductance vs current, test #8.

the experimental inductor current waveforms measured by the MADMIX. For each test, Table X summarizes the corresponding measured and estimated inductor power loss, and the errors E_k^I , E_k^Δ , E_k^P , where E_k^P is the power loss error, defined as follows:

$$E_k^P = 100 \frac{|\hat{p}_k - p_k|}{p_k} \quad (17)$$

For the given operating conditions, the adopted loss model is able to estimate \hat{p}_k with errors E_k^P lower than 1.1% for inductor #1 and 6% for inductor #2. For both inductors, the resulting errors on current E_k^I and ripple E_k^Δ are generally lower than 5% and 10%, respectively.

For the two inductors, a comparison between the measured inductor current waveforms (black solid lines) and PSIM simulations (gray dashed lines) is shown in the left panels of Figs. 8 and 9. In the right panels of the same figures, the inductance vs current profiles (black) and the curve portions covered by the simulations (gray) are also plotted. It is worth remarking

TABLE X
PSIM SIMULATIONS vs EXPERIMENTAL DATA

Inductor #1 (MSS1260-103)					
Test #	p [W]	\hat{p} [W]	E^P [%]	E^I [%]	E^Δ [%]
1	0.293	0.296	1.1	2.6	2.5
2	1.103	1.091	1.1	2.9	8.2
3	0.214	0.215	0.3	2.4	0.2
4	1.033	1.031	0.3	3.1	1.6
Inductor #2 (DO3316T-103)					
Test #	p [W]	\hat{p} [W]	E^P [%]	E^I [%]	E^Δ [%]
5	0.349	0.341	2.1	3.2	0.4
6	0.920	0.975	6.0	4.6	3.7
7	0.188	0.185	1.7	3.2	5.0
8	0.534	0.527	1.3	3.8	3.4

TABLE XI
OPERATING CONDITIONS USED TO OBTAIN DATASETS \mathcal{S}_3 AND \mathcal{S}_4

Dataset	\mathcal{S}_3 (inductor #3)	\mathcal{S}_4 (inductor #4)
V_{in} [V]	{12, 24}	{12, 24}
I_{out} [A]	{1.5, 2, 2.5, 2.8, 3.1, 3.4}	{1, 1.2, 1.4, 1.6, 1.8, 2}
f_s [kHz]	{200, 300}	{200, 300}
D	0.5	0.5

that working conditions leading to an inductance decrease higher than 50% (e.g., the case shown in Fig. 8(d)) have been considered only to highlight the reliability of the modeling approach. In real-world SPMS applications, these extreme conditions are avoided for safety and efficiency reasons and prevented by current limit circuitry integrated in each SMPS.

V. CONCLUSIONS

This paper proposes a novel behavioral modeling approach for FC power inductors operating in SMPSs. The main strengths of the proposed behavioral approach are:

- the model allows expressing the inductance as a function of the inductor current and of the average power loss;
- a limited set of data is required to train the model;
- by combining the proposed model with a reliable power loss model, it is possible to express the inductance as a function of the SMPS operating conditions, which are much more easily measurable than core temperature;
- the model can be used to perform accurate circuit simulations of SMPSs.

These features are of paramount importance to design safe and reliable high-power-density SMPSs, which exploit inductors operating beyond the weak-saturation region, in order to reduce their size and weight. The proposed inductance model accurately describes the behavior of soft-ferrite materials, commonly used in SMPS design due to their low power losses. The same power-based modeling approach can be applied to other types of materials with different inductance profiles, e.g., for powdered inductors, which show a quasi-linear inductance decrease as the current increases. The model can also be further extended to inductors transient analysis.

APPENDIX

To further check the accuracy of the proposed inductance model, two additional inductors have been considered, with the same core as for the shielded MSS1260 and the unshielded

TABLE XII
COEFFICIENT VECTORS \mathbf{x}^* FOR INDUCTORS #3 AND #4

Inductor	\mathbf{x}^*
#3	[53.45 μ H, 2.64 μ H, 3.15A $^{-1}$, -0.62AW $^{-1}$, 3.72A]
#4	[45.79 μ H, 8.27 μ H, 10.72A $^{-1}$, -0.61AW $^{-1}$, 1.95A]

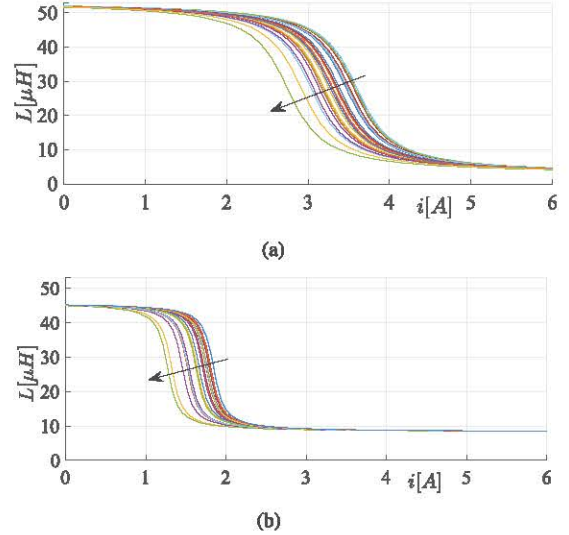


Fig. 10. Family of $L(i)$ characteristics for inductor #3 (a) and #4 (b). The arrows indicate the increasing direction of p .

TABLE XIII
STATISTICS OF THE ERRORS FOR INDUCTORS #3 AND #4

Inductor #3 (MSS1260-473)		
\bar{E}^Φ [%]	σ^Φ [%]	E_M^Φ [%]
1.62	0.43	3.49
Inductor #4 (DO3316T-473)		
\bar{E}^Φ [%]	σ^Φ [%]	E_M^Φ [%]
2.05	0.45	3.89

DO3316 families, but with nominal inductance of 47 μ H. These new samples are the MSS1260-473 (inductor #3) and the DO3316T-473 (inductor #4). Two datasets have been considered for inductors #3 and #4, labeled as \mathcal{S}_3 and \mathcal{S}_4 , respectively, consisting of $K = 24$ different operating conditions given by all the combinations of parameters V_{in} , I_{out} , f_s and D listed in Table XI. The problem (7) has been solved on datasets \mathcal{S}_3 and \mathcal{S}_4 , yielding the coefficient vectors \mathbf{x}^* shown in Table XII.

The resulting family of arctangent curves $L(i, p)$ is shown in Fig. 10. As expected, the inductance drop for inductor #3 is smoother and happens at a larger current with respect to inductor #4. Table XIII shows the statistics of the resulting modeling errors for inductors #3 and #4. Similarly to the results obtained for inductors #1 and #2, the model errors for inductor #4 are higher than for inductor #3.

REFERENCES

- [1] J. W. Kolar *et al.*, "PWM converter power density barriers," in *Proc. Power Convers. Conf.*, Nagoya, Japan, Apr. 2007, pp. 9–29.
- [2] Q. Li *et al.*, "Technology road map for high frequency integrated DC-DC converter," in *Proc. 25th Annu. IEEE Appl. Power Electron. Conf. Expo. (APEC)*, Feb. 2010, pp. 533–539, doi: 10.1109/APEC.2010.5433619.
- [3] C. Ó. Mathúna, N. Wang, S. Kulkarni, and S. Roy, "Review of integrated magnetics for power supply on chip (PwrSoC)," *IEEE Trans. Power Electron.*, vol. 27, no. 11, pp. 4799–4816, Nov. 2012.

- [4] G. Di Capua, N. Femia, and K. Stoyka, "Switching power supplies with ferrite inductors in sustainable saturation operation," *Int. J. Elect. Power Energy Syst.*, vol. 93, pp. 494–505, Dec. 2017.
- [5] L. Milner and G. A. Rincón-Mora, "Small saturating inductors for more compact switching power supplies," *IEEE Trans. Elect. Electron. Eng.*, vol. 7, no. 1, pp. 69–73, 2012.
- [6] C. Wilhelm, D. Kranzer, and B. Burger, "Development of a highly compact and efficient solar inverter with silicon carbide transistors," in *Proc. 6th Int. Conf. Integr. Power Electron. Syst. (CIPS)*, Mar. 2010, pp. 1–6.
- [7] A. Stadler, T. Stolzke, and C. Gulden, "Nonlinear power inductors for large current crest factors," in *Proc. Eur. Power Convers. Intell. Motion Conf.*, May 2012, pp. 1548–1553.
- [8] Panasonic Industry Europe. *Power Choke Coils for Automotive Applications*. Accessed: Jan. 2, 2019. [Online]. Available: <https://eu.industrial.panasonic.com/node/2539/power-choke-coils-automotive-applications>
- [9] G. Di Capua, N. Femia, and K. Stoyka, "Differential evolution algorithm-based identification of ferrite core inductors saturation curves," in *Proc. IEEE 13th Int. Conf. Ind. Inform.*, Jul. 2015, pp. 1636–1641.
- [10] A. Oliveri, M. Lodi, and M. Storace, "Accurate modeling of inductors working in nonlinear region in switch-mode power supplies with different load currents," in *Proc. 15th Int. Conf. Synth., Modeling, Anal. Simulation Methods Appl. Circuit Design*, Jul. 2018, pp. 1–4.
- [11] G. Di Capua and N. Femia, "A novel method to predict the real operation of ferrite inductors with moderate saturation in switching power supply applications," *IEEE Trans. Power Electron.*, vol. 31, no. 3, pp. 2456–2464, Mar. 2016.
- [12] F. Bizzarri, A. Brambilla, L. Codecasa, and S. Callegari, "On the benefit of adopting saturable inductors in switching-mode power-supplies: A case study," in *Proc. IEEE Int. Symp. Circuits Syst.*, May 2018, pp. 1–5.
- [13] H. Gurleyen, E. Mese, J. H. Kim, and B. Sarioglu, "Nonlinear analytical model of an inductance considering saturation and temperature variation," in *Proc. IEEE Energy Convers. Congr. Expo.*, Oct. 2017, pp. 3150–3154.
- [14] *Current Temperature Ratings*, document 361-1, Coilcraft, Inc., 2014. [Online]. Available: www.coilcraft.com/pdfs/Doc361_Current_Temp.pdf
- [15] L. O. Chua, *Introduction to Nonlinear Network Theory*. New York, NY, USA: McGraw-Hill, 1969.
- [16] K. Stoyka, G. Di Capua, and N. Femia, "A novel AC power loss model for ferrite power inductors," *IEEE Trans. Power Electron.*, to be published. [Online]. Available: <https://ieeexplore.ieee.org/abstract/document/8386705>, doi: 10.1109/TPEL.2018.2848109.
- [17] *Shielded Power Inductors MSS1260*, document 361-1, Coilcraft, Inc., 2014. [Online]. Available: <https://www.coilcraft.com/pdfs/mss1260.pdf>
- [18] *Power Inductor Analysis & Comparison Tool*, document 361-1, Coilcraft, Inc., 2014. [Online]. Available: www.coilcraft.com/apps/power_tools/compare/
- [19] J. D. Pollock, W. Lundquist, and C. R. Sullivan, "Predicting inductance roll-off with DC excitations," in *Proc. IEEE Energy Convers. Congr. Expo.*, Sep. 2011, pp. 2139–2145.
- [20] W. A. Roshen, "A practical, accurate and very general core loss model for nonsinusoidal waveforms," *IEEE Trans. Power Electron.*, vol. 22, no. 1, pp. 30–40, Jan. 2007.
- [21] M. Wens and J. Thone, *MADMIX: The Standard for Measuring SMPS Inductors*. Laboe, Germany: Bodo's Power Systems-Verlag, 2015, pp. 52–54. [Online]. Available: https://www.bodospower.com/pdf/bodos_mediakit.pdf



Alberto Oliveri (M'17) received the M.Sc. and Ph.D. degrees in electrical engineering from the University of Genoa, Genoa, Italy, in 2009 and 2013, respectively. He is currently an Assistant Professor with the Department of Electrical, Electronics and Telecommunications Engineering and Naval Architecture, University of Genoa.

His main research interests include the design and circuit implementation of explicit exact and approximate model predictive control functions and piecewise-affine virtual sensors.



Giulia Di Capua (S'06–M'13) received the B.Sc. and M.Sc. degrees (Hons.) in electronic engineering and the Ph.D. degree in information engineering from the University of Salerno, Italy, in 2006, 2009, and 2013, respectively. She is currently an Assistant Professor at the Department of Information and Electrical Engineering and Applied Mathematics, University of Salerno.

Her research interests include switching mode power supplies optimization, magnetic components design, and wireless power transfer.

She is a member of the IEEE Technical Committee on Power and Energy Circuits and Systems (TC-PECAS).



Kateryna Stoyka received the B.Sc. and M.Sc. degrees in electronic engineering from the University of Salerno, Italy, in 2011 and 2015, respectively, where she is currently pursuing the Ph.D. degree in computing and information engineering.

Her main research interests include analysis and design of switching mode power supplies, power magnetics, numerical techniques for identification, and optimization of behavioral models of power devices and systems.



Matteo Lodi was born in Genoa, Italy, in 1991. He received the Laurea (M.Sc.) five-year degree (*summa cum laude*) in electronic engineering from the University of Genoa, Genoa, in 2015, where he is currently pursuing the Ph.D. degree in electrical engineering. He was a visitor to Georgia State University, Atlanta, GA, USA, in 2016.

His main research interests are in the area of modeling of nonlinear systems (hysteresis and networks of biological neurons), bifurcation analysis, and nonlinear dynamics.



Marco Storace (M'01–SM'14) was born in Genoa, Italy, in 1969. He received the Laurea (M.Sc.) five-year degree (*summa cum laude*) in electronic engineering and the Ph.D. degree in electrical engineering from the University of Genoa, Genoa, in 1994 and 1998, respectively. Since 2011, he has been a Full Professor with the University of Genoa. He was a visitor to EPFL, Lausanne, Switzerland, in 1998 and 2002.

He is the author or coauthor of more than 140 scientific papers, more than an half of which have been published in international journals. His main research interests are in the area of nonlinear circuit theory and applications, with emphasis on models of nonlinear systems (e.g., hysteresis and biological neurons), methods for the piecewise-linear approximation of nonlinear systems, bifurcation analysis, and nonlinear dynamics.

He served as an Associate Editor for the IEEE TRANSACTIONS ON CIRCUITS AND SYSTEMS—II from 2008 to 2009. He is a Secretary of the IEEE Technical Committee on Nonlinear Circuits and Systems (TC-NCAS).



Nicola Femia (M'94–SM'13) received the Laurea degree (Hons.) in industrial technologies engineering from the University of Salerno, Italy, in 1988.

He is currently a Full Professor with the University of Salerno, where he teaches power electronics and energetic intelligence, in the Electronic Engineering and Computer Engineering Master Programs, and leads the Power Electronics and Renewable Sources Laboratory. He has co-authored six patents and over 190 scientific papers on power electronics topics, published in international journals and proceedings

of international conferences.

In 2014, he has been a Visiting Professor with the Department of Electrical Engineering, Stanford University, Stanford, CA, USA.

He served as an Associate Editor for the IEEE TRANSACTIONS ON POWER ELECTRONICS from 1995 to 2003.